

Galaxy properties as revealed by MaNGA. III. Kinematic profiles and stellar population gradients in S0s

H. Domínguez Sánchez^{1,2*}, M. Bernardi^{1†}, F. Nikakhtar¹, B. Margalef-Bentabol¹ and R. K. Sheth¹

¹ *Department of Physics and Astronomy, University of Pennsylvania, Philadelphia, PA 19104, USA*

² *Institute of Space Sciences (ICE, CSIC), Campus UAB, Carrer de Magrans, E-08193 Barcelona, Spain*

1 November 2021

ABSTRACT

This is the third paper of a series where we study the stellar population gradients (SP; ages, metallicities, α -element abundance ratios and stellar initial mass functions) of early type galaxies (ETGs) at $z \leq 0.08$ from the MaNGA-DR15 survey. In this work we focus on the S0 population and quantify how the SP varies across the population as well as with galactocentric distance. We do this by measuring Lick indices and comparing them to stellar population synthesis models. This requires spectra with high signal-to-noise which we achieve by stacking in bins of luminosity (L_r) and central velocity dispersion (σ_0). We find that: 1) There is a bimodality in the S0 population: S0s more massive than $3 \times 10^{10} M_\odot$ show stronger velocity dispersion and age gradients (age and σ_r decrease outwards) but little or no metallicity gradient, while the less massive ones present relatively flat age and velocity dispersion profiles, but a significant metallicity gradient (i.e. $[M/H]$ decreases outwards). Above $2 \times 10^{11} M_\odot$ the number of S0s drops sharply. These two mass scales are also where global scaling relations of ETGs change slope. 2) S0s have steeper velocity dispersion profiles than fast rotating elliptical galaxies (E-FRs) of the same luminosity and velocity dispersion. The kinematic profiles and stellar population gradients of E-FRs are both more similar to those of slow rotating ellipticals (E-SRs) than to S0s, suggesting that E-FRs are not simply S0s viewed face-on. 3) At fixed σ_0 , more luminous S0s and E-FRs are younger, more metal rich and less α -enhanced. Evidently for these galaxies, the usual statement that ‘massive galaxies are older’ is not true if σ_0 is held fixed.

Key words: galaxies: fundamental parameters – galaxies: spectroscopy – galaxies: structure

1 INTRODUCTION

The properties of early type galaxies (hereafter ETGs) provide insight into their assembly and evolutionary paths, being crucial for our understanding of galaxy formation. In particular, the formation mechanisms of the S0 population are still debated. Many key properties of the stellar population of a galaxy – the total mass in stars, the mean stellar age, star formation history, chemical composition (metallicity, α -element abundance ratios, dust content) and the Initial Mass Function (hereafter IMF) – are encoded in its spectrum (Worthey 1994; Trager et al. 1998; Kauffmann et al. 2003; Bernardi et al. 2006; Panter et al. 2007; Thomas et al.

2011; Vazdekis et al. 2015; Tang & Worthey 2017; Conroy et al. 2018).

While there are clear correlations between the stellar populations of galaxies and their morphology, even amongst just ETGs, the stars in more massive galaxies tend to be older, more metal rich, more α -enhanced (implying that they formed their stars over a shorter timescale) (e.g. Thomas et al. 2005), with velocity dispersion driving many of the observed correlations (e.g. Bernardi et al. 2005). These changes contribute to the observed scaling relations between half-light radius, velocity dispersion and stellar mass. In particular, curvature in these scaling relations (e.g. Bernardi et al. 2011) is thought to indicate changes in the stellar population and assembly history across the early-type population.

Moreover, there are stellar population variations even within a single galaxy. The stellar population gradient (i.e.,

* E-mail: dominguez@ice.csic.es

† bernardm@sas.upenn.edu

the correlation between stellar population and distance from the center) contains hints about the assembly history and is expected to constrain inside-out versus outside-in and in-situ versus ex-situ formation scenarios (Parikh et al. 2019; Ferreras et al. 2019; Lacerna et al. 2020). These gradients are revealed thanks to Integral Field Unit surveys – such as the one used in this work, MaNGA (Bundy et al. 2015) – which provide spatially resolved spectra for individual galaxies.

One of the goals of the present study is to see if we can decode the story that is encoded both in the curvature of scaling relations and in SP gradients. In Papers I and II of this series (Domínguez Sánchez et al. 2019; Bernardi et al. 2019) we analyzed the stellar population gradients from stacked spectra of slow and fast rotator elliptical galaxies (hereafter E-SRs and E-FRs). The main goal here is to study the gradients in S0s.

Previous work suggests that whereas more luminous S0s have been formed at high redshift by violent, dissipative processes, less luminous lenticulars have been formed by secular processes gently stripping gas from spiral discs (Barway et al. 2007, 2009). More recent work suggests that the bulges of high-mass, old, and metal-rich S0s are older than their discs, while the bulges of young, metal-poor and lower mass S0s are slightly younger than their discs (Fraser-McKelvie et al. 2018, FM2018 hereafter). We would like to see how our data align with these findings. Our study is also motivated by the suggestion that the distinction between fast rotator ellipticals and S0s is artificial: that E-FRs are simply S0s viewed face-on (Cappellari 2016; Graham et al. 2019). The stacked spectra in Papers I and II did not allow a clear test of this assertion. Therefore, a secondary goal here is to check if the kinematic profiles, stellar populations and SP gradients of E-FRs and S0s are similar.

Section 2 discusses how we select our sample, and the relevant photometric, spectroscopic and morphological information available to us. It also compares the global scaling relations (how size and velocity dispersion vary with stellar mass) of S0s with those of E-FRs and E-SRs. Whereas this comparison does not use any information from gradients or stellar population modeling, Section 3 measures gradients in the kinematics and the chemical abundances of S0s. It then uses the measured chemical abundances to constrain the stellar populations (light-weighted age, metallicity, α -enhancement, IMF) of S0s. To check if E-FRs are simply face-on S0s, Section 4 performs a similar analysis of E-FRs which are selected to have similar luminosities and velocity dispersions as our S0s. Section 5 discusses our results in the context of previous work, especially how our analysis of gradients compares with the bulge-disk analysis of FM2018. A final section summarizes our findings.

2 DATA

2.1 MaNGA survey and photometry

The MaNGA survey (Bundy et al. 2015; Drory et al. 2015; Law et al. 2015, 2016; Yan et al. 2016a,b) is a component of the Sloan Digital Sky Survey IV (Gunn et al. 2006; Smee et al. 2013; Blanton et al. 2017; hereafter SDSS IV) using integral field units (IFUs) to measure spectra across ~ 10000 nearby galaxies. The MaNGA selection function, while com-

plicated, is well defined (Wake et al. 2017). In what follows, when we refer to ‘weighted’ quantities, the weight is ESWEIGHT from Wake et al. (2017).

In this work, as in Papers I and II, we use the MaNGA DR15 (Westfall et al. 2019; Aguado et al. 2019; Fischer et al. 2019). The photometric parameters we use come from the PyMorph Photometric Value Added Catalogue (MPP-VAC) presented in Fischer et al. (2019), which provides photometric parameters from Sérsic and Sérsic + Exponential fits (we use the ‘truncated’ magnitudes and sizes). We refer the reader to the corresponding references for further details on the observations and photometric reductions.

2.2 Sample selection: Morphology

This paper uses a clean sample of S0 galaxies to study their properties as a function of global parameters (i.e. absolute magnitude, central velocity dispersion) as well as galactocentric distance (i.e. their gradients).

To select our S0 sample we use the Deep Learning Morphological Value Added Catalog (Fischer et al. 2019, MDLM-VAC) that provides morphological properties derived from supervised Deep Learning algorithms based on Convolutional Neural Networks (see Domínguez Sánchez et al. 2018 for more details). The selection requires

$$\text{TType} \leq 0 \quad \text{and} \quad P_{\text{S0}} > 0.5.$$

The first condition selects early-type galaxies (1948 observations of 1908 galaxies) instead of late-type galaxies, and the second selects S0s (896 observations of 880 galaxies) rather than Es. About $\sim 20\%$ of the MaNGA DR15 galaxies are S0s. Some previous work uses results from the Galaxy Zoo2 analysis (Willett et al. 2013; Hart et al. 2016) to select lenticulars. This can result in a sample in which Spirals contribute as much as 40% (e.g. see Figs.24-26 in Fischer et al. 2019). In contrast, objects identified by the MDLM-VAC as S0s are significantly less likely to be Spirals (also see Section 5). To illustrate, we show a random selection of images in the Appendix.

In addition, the IFU observations provided by MaNGA enable an estimate of the angular momentum λ_e defined in Emsellem et al. (2007) (corrected for seeing following Graham et al. 2018) for each galaxy. When combined with the ellipticity ϵ returned by the MPP-VAC, this allows us to separate slow from fast rotating galaxies (e.g. Paper II). This $\lambda_e - \epsilon$ diagnostic shows that the vast majority of S0s are FRs (see Figs. 28–30 in Fischer et al. 2019). While this is not surprising, it is reassuring, as the angular momentum played no role in the MDLM-VAC morphological classification. Although, in principle, E-FRs can have $\lambda_e < 0.2$, in what follows, when we show E-FRs, they have $\lambda_e > 0.2$ unless we specify otherwise. This is similar to our convention in Papers I and II.

2.3 Curvature in scaling relations

Before we analyse the stellar populations of our S0 sample, Figure 1 shows updated versions of plots which first appeared in Bernardi et al. (2011), highlighting the presence of two mass scales in the early-type galaxy population: $3 \times 10^{10} M_{\odot}$ and $2 \times 10^{11} M_{\odot}$. (Following Paper I, we define

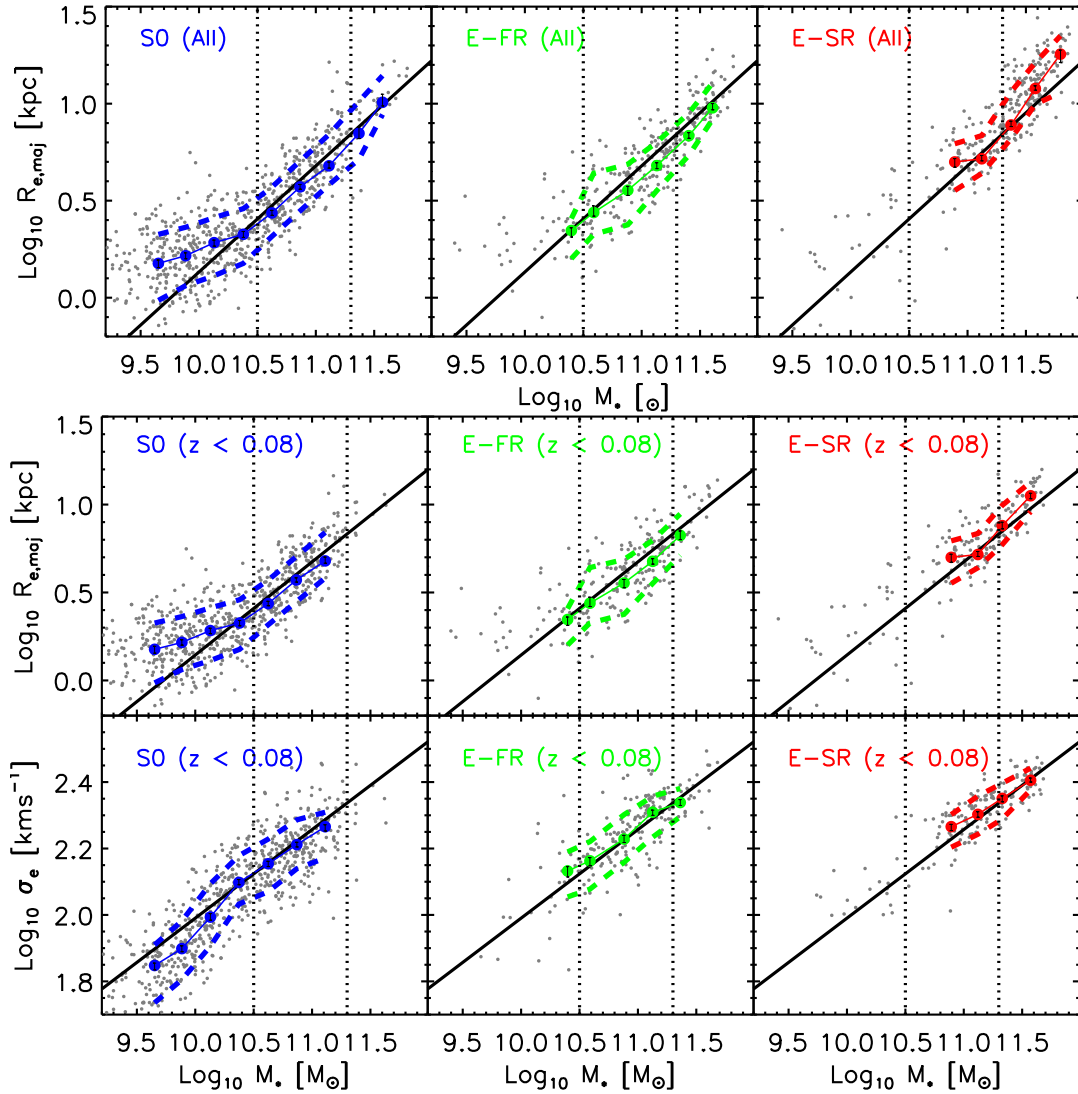


Figure 1. Correlation of stellar mass with size (top and middle) and velocity dispersion (bottom) for S0s (left), E-FRs with $\lambda_e > 0.2$ (middle) and E-SRs (right) in MaNGA. Middle panels show the subset of the objects in the top panels which have $z < 0.08$. Solid black lines in each panel show linear fits to the full sample (S0 + E-FR + E-SR) in the mass range $10.5 \leq \log_{10} M_*/M_\odot \leq 11.3$, while colored curves show the median and quartiles of each subsample. Dotted vertical lines show two mass scales at which the scaling relations curve away from this linear fit; this curvature is thought to reflect changes in the typical formation or assembly history. Above $2 \times 10^{11} M_\odot$ dry mergers are expected to dominate; here, the fraction of S0s drops sharply and Es dominate the counts (Table 1). Below $3 \times 10^{10} M_\odot$ S0s dominate. The remainder of this paper studies if the stellar populations and/or assembly histories of S0s change dramatically around $3 \times 10^{10} M_\odot$.

MORPHOLOGICAL FRACTIONS AT FIXED M_*

M_* [$10^{10} M_\odot$]	S0	E-FR $\lambda_e > 0.2$	E-FR $\lambda_e < 0.2$	E-SR
> 20	0.14	0.28	0.17	0.41
3 – 20	0.60	0.23	0.06	0.11
0.1 – 3	0.87	0.07	0.01	0.05

Table 1. Morphological fractions in the specified mass bin, weighted by the MaNGA selection function, in each of three mass bins shown in Figure 1.

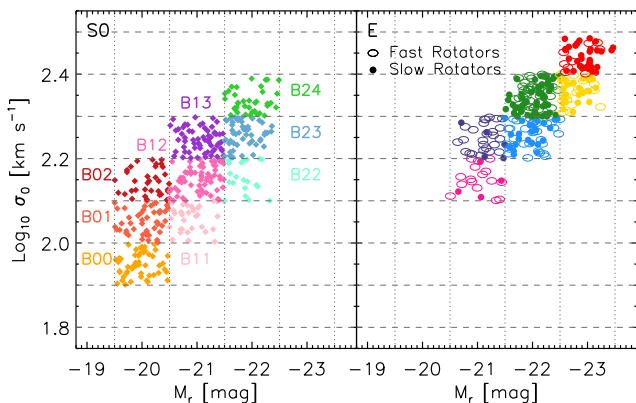
M_* as the product of M_*/L_r from Mendel et al. 2014, and L_r from the MPP-VAC.) The difference here is that we have used the MDLM-VAC classifications to separate the early-

type population into S0s (left), E-FRs (with $\lambda_e > 0.2$; middle) and E-SRs (right). The top and middle panels show the R_e - M_* correlation; they only differ because of a redshift cut. This redshift cut matters more for the E-SRs than for the S0s, which are the subject of this paper. We have included the top panel since there are too few E-SRs at $z < 0.08$ to see the change in curvature at $2 \times 10^{11} M_\odot$ clearly. The bottom panels show the σ_e - M_* relation for the objects at $z < 0.08$. The vertical dotted lines identify the mass scales at which the scaling relations change.

The MaNGA selection algorithm is complicated, so Figure 1 and the following figures show results when galaxies have been weighted by ESWEIGHT to account for the MaNGA selection. We note that since most of our analysis is done in narrow mass bins the effect of weighting is negligible except

M_* DISTRIBUTION AT FIXED MORPHOLOGY

Sample	$M_* = 0.1 - 3$ [$10^{10} M_\odot$]	$3 - 20$ [$10^{10} M_\odot$]	> 20 [$10^{10} M_\odot$]
Observed $z < 0.08$			
E-SR	0.10	0.48	0.42
E-FR ($\lambda_e < 0.2$)	0.11	0.55	0.34
E-FR ($\lambda_e > 0.2$)	0.11	0.69	0.20
S0	0.48	0.49	0.03
Observed All			
E-SR	0.06	0.28	0.66
E-FR ($\lambda_e < 0.2$)	0.08	0.42	0.50
E-FR ($\lambda_e > 0.2$)	0.09	0.53	0.38
S0	0.44	0.49	0.07
Weighted			
E-SR	0.30	0.52	0.18
E-FR ($\lambda_e < 0.2$)	0.27	0.60	0.13
E-FR ($\lambda_e > 0.2$)	0.24	0.68	0.08
S0	0.65	0.34	0.01

Table 2. Stellar mass distribution for the different morphological types in the $z < 0.08$ sample, the full sample, and when objects have been weighted to account for the MaNGA selection function.**Figure 2.** Distribution of central velocity dispersion σ_0 and absolute magnitude M_r for S0s (left) and Es (right). Filled and open ellipses in the right hand panel show slow and fast rotator Es. FRs dominate at fainter luminosities; essentially all the S0s are FRs. Grid shows the values of M_r and σ_0 which define the bins in (Table 3). The label B_{ms} , where m denotes the magnitude and s the σ_0 , indicates the bin reported in Table 3.

for when we compare the observed counts in one mass bin with those in another (see Table 2).

Table 1 shows the morphological fractions in fixed mass bins, weighted by **ESWEIGHT**. These weighted counts show that S0s account for more than 85% of the sample below $3 \times 10^{10} M_\odot$, but less than 15% above $2 \times 10^{11} M_\odot$. In contrast, E-SRs are only about 5% of the objects below $3 \times 10^{10} M_\odot$ but about 40% of the objects above $2 \times 10^{11} M_\odot$. (These fractions do not depend on the redshift cut.)

While it is tempting to attribute some of the change in scaling relations at these mass scales to morphology, it is important to note that, even in the S0 population, the scaling relations change dramatically at $3 \times 10^{10} M_\odot$. Papers I

BINNING OF GALAXIES

Bin	M_r [mag]	$\text{Log}_{10} \sigma_0$ [km s^{-1}]	S0 Galaxies $z \leq 0.08$	S0 Galaxies all z
B00	-19.5, -20.5	1.90, 2.00	50	50
B01	-19.5, -20.5	2.00, 2.10	49	49
B02	-19.5, -20.5	2.10, 2.20	36	36
B11	-20.5, -21.5	2.00, 2.10	35	35
B12	-20.5, -21.5	2.10, 2.20	63	64
B13	-20.5, -21.5	2.20, 2.30	63	63
B22	-21.5, -22.5	2.10, 2.20	22	23
B23	-21.5, -22.5	2.20, 2.30	55	63
B24	-21.5, -22.5	2.30, 2.40	37	39

Table 3. Bin definitions and number of S0s in each bin, with and without redshift cut.

and II studied the E-FR and E-SR galaxies. In what follows, we will perform a similar study of the S0s, paying particular attention to SPs and gradients above and below $3 \times 10^{10} M_\odot$.

Before moving on, Table 2 shows the range of stellar masses M_* spanned by the different morphological types. Here, the weighted fractions are the most relevant: they show that only about a third of E-SRs have $M_* < 3 \times 10^{10} M_\odot$, whereas nearly two-thirds of S0s have such masses. In addition, about 20% of E-SRs but essentially no S0s have $M_* > 2 \times 10^{11} M_\odot$.

2.4 Sample selection: Binning in σ_0 and L_r

We remove from our sample galaxies with no available photometric parameters (FLAG_FIT=3 in MPP-VAC), or with unreliable spectra due to contamination by neighbours (identified by visual inspection). We also limited our sample to galaxies with $z \leq 0.08$ and $R_e < 15$ arcsec, for reasons we discuss in Paper I. Note that the redshift cut has little impact: it only removes 12 S0 galaxies, 11 of which have $M_r < -21.5$ (see Table 3).

To measure absorption features accurately, in particular the TiO indices associated with IMF variations, spectra must have $\text{SN} \geq 100$. As we discussed in Paper I, this requires to create stacked spectra. We do so by first binning in central velocity dispersion σ_0 and absolute magnitude M_r . The bin limits and the number of galaxies in each bin are given in Table 3. The left hand panel of Figure 2 shows how the S0s (colored symbols) populate the 9 bins (grids). For comparison, the right hand panel shows the distribution of slow and fast rotating Es. Papers I and II considered the objects in the four brightest bins in the right hand panel. Although our main focus here is on the S0s, in Section 4 we compare S0s with E-FRs.

3 GRADIENTS IN THE S0 SAMPLE

3.1 Velocity dispersion

To measure SP gradients we follow the same methodology as in Paper I (see section 2.3 there). Briefly, for each M_r and σ_0 bin, we compute stacked spectra from concentric ellipsoidal shells that have width $0.1 R_{e,\text{maj}}$ along the major axis (so they are b/a thinner along the minor axis). The stacked

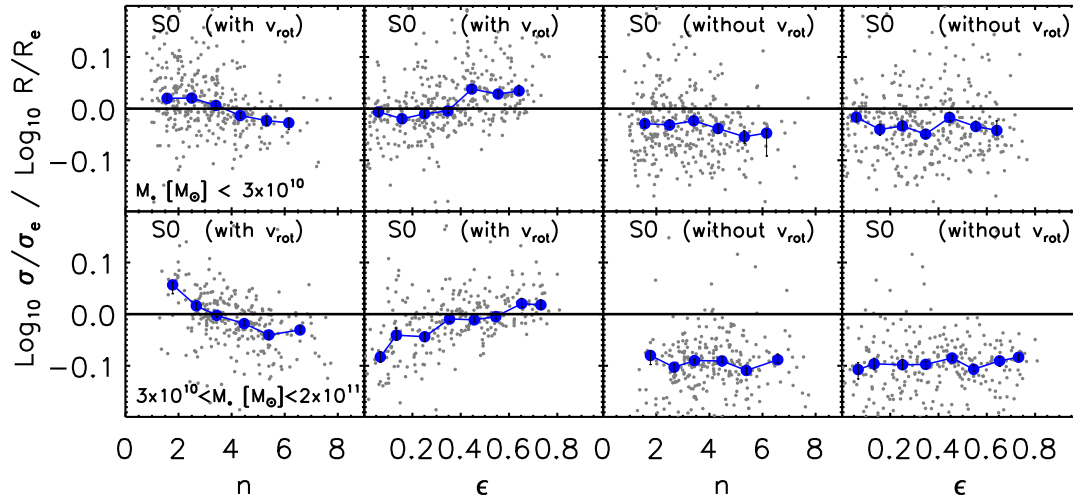


Figure 3. Velocity dispersion gradient for low (top) and high (bottom) mass S0s, shown as a function of Sersic index n and ellipticity ϵ . In left hand panels, estimated dispersions include a contribution from rotation; in right hand panels, this rotation has been removed. In all panels, symbols show individual galaxies and curves show the trend defined by the median value.

value is the median rest-frame normalized flux of all the individual spaxels from MAPS-VOR10-GAU-MILES_{HC} with $S/N > 5$ which belong to each radial bin. To avoid variations due to the spectral slope, the normalization is done in the continuum region of each of the lick indices that we measure (defined in Table 3 of Paper I). The spectra are then smoothed to a common resolution of 300 km s^{-1} to allow for a fair comparison between the different bins and the values from stellar population synthesis models.

To bring them to the 300 km s^{-1} resolution, we first need to measure the velocity dispersion of each stack. The velocity dispersion varies with galactocentric distance. We illustrate this gradient by taking the ratio of $\log_{10}[\sigma(< R_{\min})/\sigma(< R_{\max})]$ to $\log_{10}(R_{\min}/R_{\max})$ (Figure 3). Where possible, we set $R_{\min} = R_e/4$ and $R_{\max} = R_e$. However, for some galaxies, the angular size corresponding to $R_e/4$ is less than 1.2 arcsec, so seeing is an issue. For these we set $R_{\min} = R_e/2$. For a few other galaxies, the available spectra do not extend all the way out to R_e . For these, we set $R_{\max} = 3R_e/4$. Our notation $\sigma(< R)$ means we estimate σ from a stacked spectrum constructed using all the available spaxels within R . We can do this in two ways: either by simply stacking all the spaxels directly (as this approximates what would have been observed by a large fiber), or by first removing the mean rotation speed from each spaxel before stacking.

Figure 3 shows the gradients measured in this way as a function of Sersic index n and image ellipticity ϵ (a face-on disk would have $\epsilon = 0$) for low (top) and high (bottom) mass S0s. There are clear trends with both n and ϵ when rotation is included in the dispersion estimate (left hand panels). These trends are not present when rotation has been removed (right hand panels). Clearly, removing rotation is preferable. Comparison of the top-right and bottom-right panels shows that, once rotation has been removed, the more massive S0s clearly have larger gradients. Thus, from the velocity dispersion profiles alone, we already have a hint that the mass scale $3 \times 10^{10} M_{\odot}$, so apparent in Figure 1, is special.

Figure 4 shows the full velocity dispersion profile for each bin after removing the mean rotation speed from each

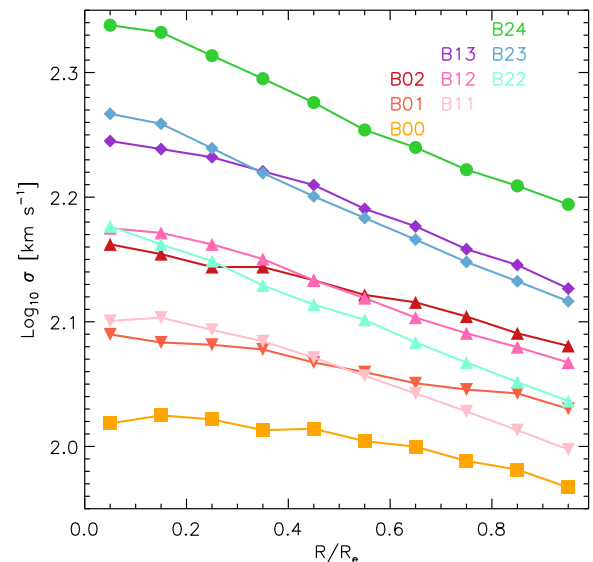


Figure 4. Velocity dispersion profiles obtained from the stacked spectra of the S0 sample. Colors correspond to the bins presented in Figure 2, as stated in the legend (the same symbols are used for bins with the same σ_0). S0s with larger σ_0 have steeper profiles and, for the same σ_0 , more luminous galaxies have steeper profiles.

spaxel before stacking. It is easy to see that the profiles are steep at larger σ_0 values and, at fixed σ_0 , steeper for the brightest galaxies (compare the cyan with the dark red lines). In fact, the fainter ($M_r > -20.5$) S0s show a much flatter velocity dispersion profile – consistent with Figure 3 (right panels) – which, we will show in the next sections, comes along with a strong gradient in metallicity but almost no age gradient.

3.2 Lick indices and SSP models

For each stack, we measure a set of Lick indices which we compare to the predictions of the MILES SSP models (Vazdekis et al. 2010) to estimate age, metallicity, α -

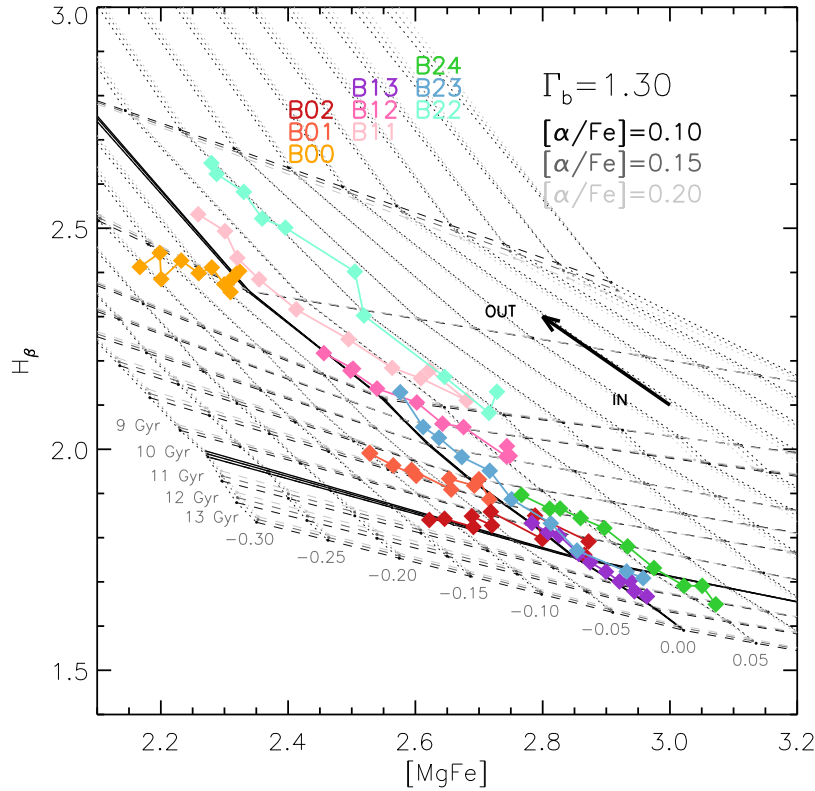


Figure 5. Lick index H_β versus $[MgFe]$ diagram for the S0 sample. Colored symbols show measurements from the stacked spectra in each bin at different galactocentric distances as indicated by the arrow. These are superimposed on age-metallicity grids from the MILES-Padova models with other SP parameters as indicated. Model grids all have same IMF slope ($\Gamma_b = 1.30$) but different α -enhancement values (shown as different grey scales – the grids are nearly identical).

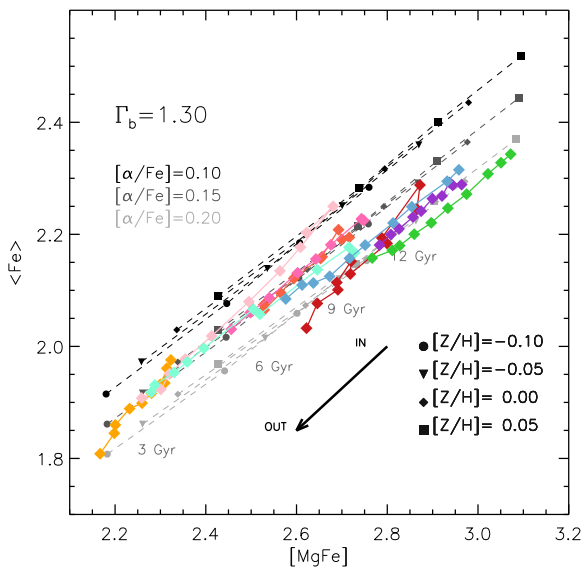


Figure 6. Same as Figure 5 but now for $\langle Fe \rangle$. Model grids again all have $\Gamma_b = 1.3$, but the dependence on α -enhancement is much stronger.

enhancement, IMF slope and M_*/L . In particular, we use three index-index diagrams to constrain our parameter space: H_β - $[MgFe]$ is sensitive to age and metallicity, $\langle Fe \rangle$ - $[MgFe]$ is sensitive to the α -enhancement and $TiO2_{SDSS}$ -

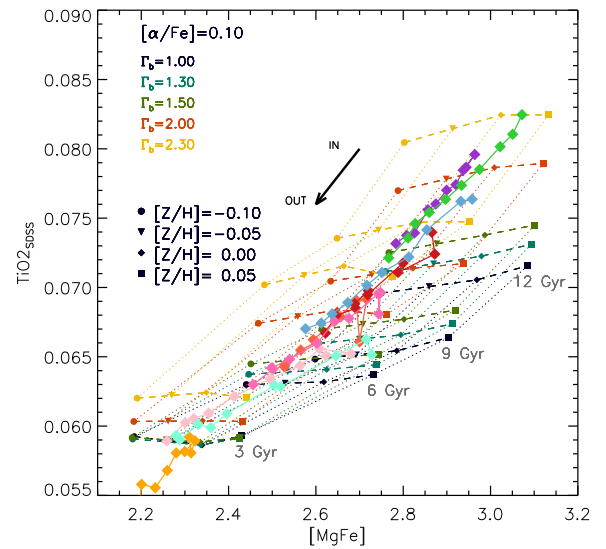


Figure 7. Same as Figure 5 but now for $TiO2_{SDSS}$. In this case, $[\alpha/Fe]$ is fixed to 0.10 and grids with different IMF slopes are shown, color-coded according to the legend.

$[MgFe]$ is a good IMF indicator. The indices are defined following Trager et al. (1998), except for $TiO2_{SDSS}$ which was introduced by La Barbera et al. (2013) (see Table 3 from Paper I).

We use the MILES-Padova models with BiModal IMFs

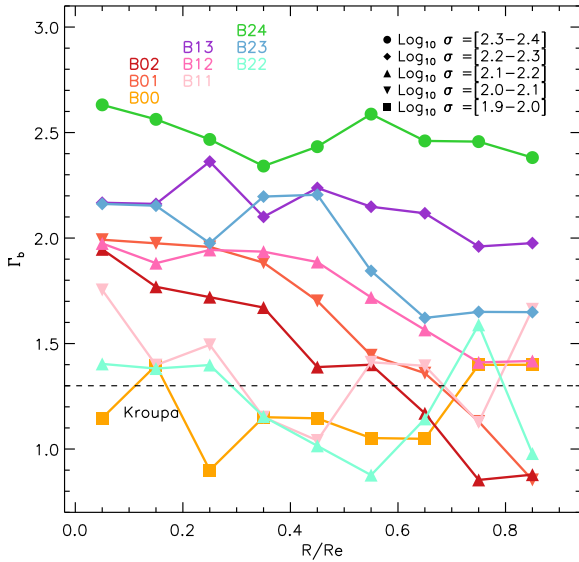


Figure 8. Best-fitting IMF slope as a function of galactocentric distance. Colors represent the bins defined in Figure 2; symbols indicate the value of σ_0 . The IMF slope is estimated by comparing the Lick indices, especially $\text{TiO2}_{\text{SDSS}}$, with the MILES bimodal IMF SSP models. The horizontal dashed line indicates the Kroupa IMF.

to interpret our measurements. Our results depend on a number of assumptions such as the choice of SSP models, the IMF parametrisation or the indices used as IMF indicators, as discussed in the Appendix of Paper I. To ease the comparison with the results from Paper I and II, we use exactly the same methodology (including SSP library, α -enhancement correction of the MILES-Padova models and best-fitting procedure) explained in detail in Section 3 of Paper I. In Paper I we also discussed the impact of variations in $[\text{X}/\text{Fe}]$ elements when constraining IMF slopes (Figure 12 from Paper I) and we tested 4 different assumptions (Figure 13 and Table 4 from Paper I). In this work we restrict our analysis to what we called assumption 3 (i.e., allowing for IMF variations for each bin and with galactocentric distance) and fixing $\Delta_{[\text{X}/\text{Fe}]} = 0.003$.

Figure 5 shows how H_β varies with $[\text{MgFe}]$: Colored symbols show the values measured for each bin and grids show the MILES SP models. There are obvious differences between the radial gradients of the fainter galaxies (red, orange, yellow) and the brighter ones: galaxies with $M_r > -20.5$ span only a small range of H_β whereas brighter galaxies span a much larger range of index strengths. Thus, even without using SSP models to interpret the measurements, the scale $M_r \sim -20.5$ (which corresponds to a mass scale $M_* \sim 3 \times 10^{10} M_\odot$) is clearly special.

Figures 6 and 7 show a similar comparison of the $\langle \text{Fe} \rangle$ - $[\text{MgFe}]$ and $\text{TiO2}_{\text{SDSS}}$ - $[\text{MgFe}]$ relations defined by the different bins. There are again obvious trends with σ_0 at fixed L_r : e.g., the $\langle \text{Fe} \rangle$ - $[\text{MgFe}]$ relations shift to larger $[\text{MgFe}]$ as σ_0 increases and $\text{TiO2}_{\text{SDSS}}$ increases with σ_0 in each L_r bin.

Comparison with the model grids in Figure 5 shows that faint galaxies show almost no age gradient and, while having mainly sub-solar metallicities, show a large metallicity gradient. In contrast, galaxies with $M_r < -20.5$ show a stronger age gradient and little if any metallicity gradient. This is our

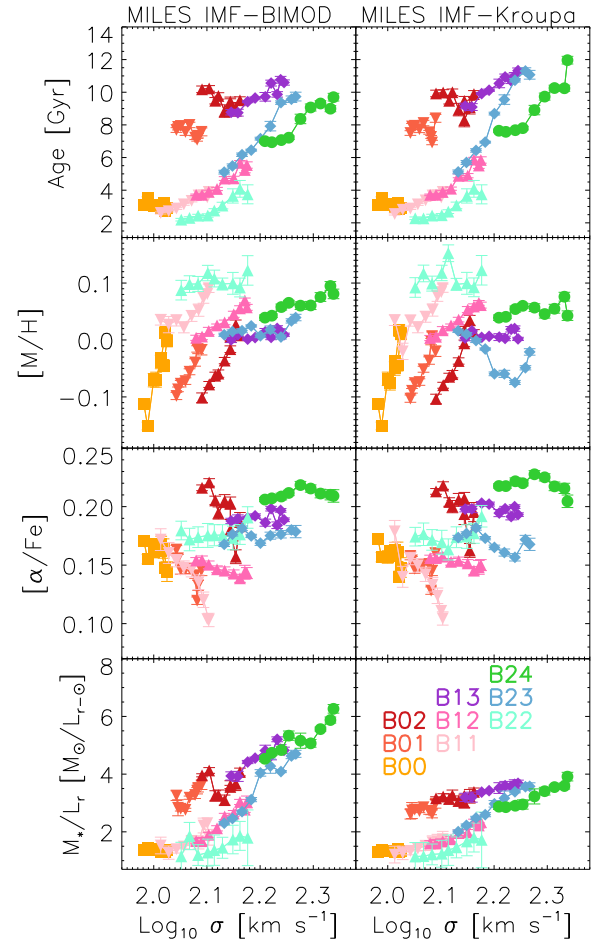


Figure 9. Best-fitting age, metallicity, α -enhancement and M_*/L_r versus σ when allowing for IMF variations (left) and when fixing the IMF to Kroupa (right). Colors represent the different bins as stated in the legend, and symbols represent the σ_0 of each bin - as in Figure 8. Error bars show uncertainties obtained by bootstrapping galaxies in each bin (see text).

first main result. In addition, the grids show that, at fixed M_r , age increases with σ_0 (orange is younger than red, pink younger than purple, cyan younger than green). Finally, the grids in Figure 6 show that, at fixed L_r , $[\alpha/\text{Fe}]$ increases with σ_0 , and those in Figure 7 suggest that the IMF slope steepens with σ_0 . We use the MILES SSP models to quantify these trends in the next subsection.

3.3 Stellar population gradients

As we did in Papers I and II, we allow for variations in the IMF slope when fitting the other SP parameters. The best-fitting IMF-slope for each bin is shown in Figure 8. There are significant differences in the IMF slope for the different populations, ranging from bottom heavy IMF ($\Gamma_b=2.5$) for galaxies with the largest L_r and σ_0 to Kroupa-like values (Kroupa 2001, $\Gamma_b=1.3$) for the other extreme (smallest L_r and σ_0). Although the radial gradients are noisy, there is a clear trend for IMF slope to decrease with decreasing σ_0 (at fixed L_r). However, galaxies with the same σ_0 do not share the same IMF slope, implying that luminosity also correlates with the IMF. Finally, IMF gradients are obvious for some

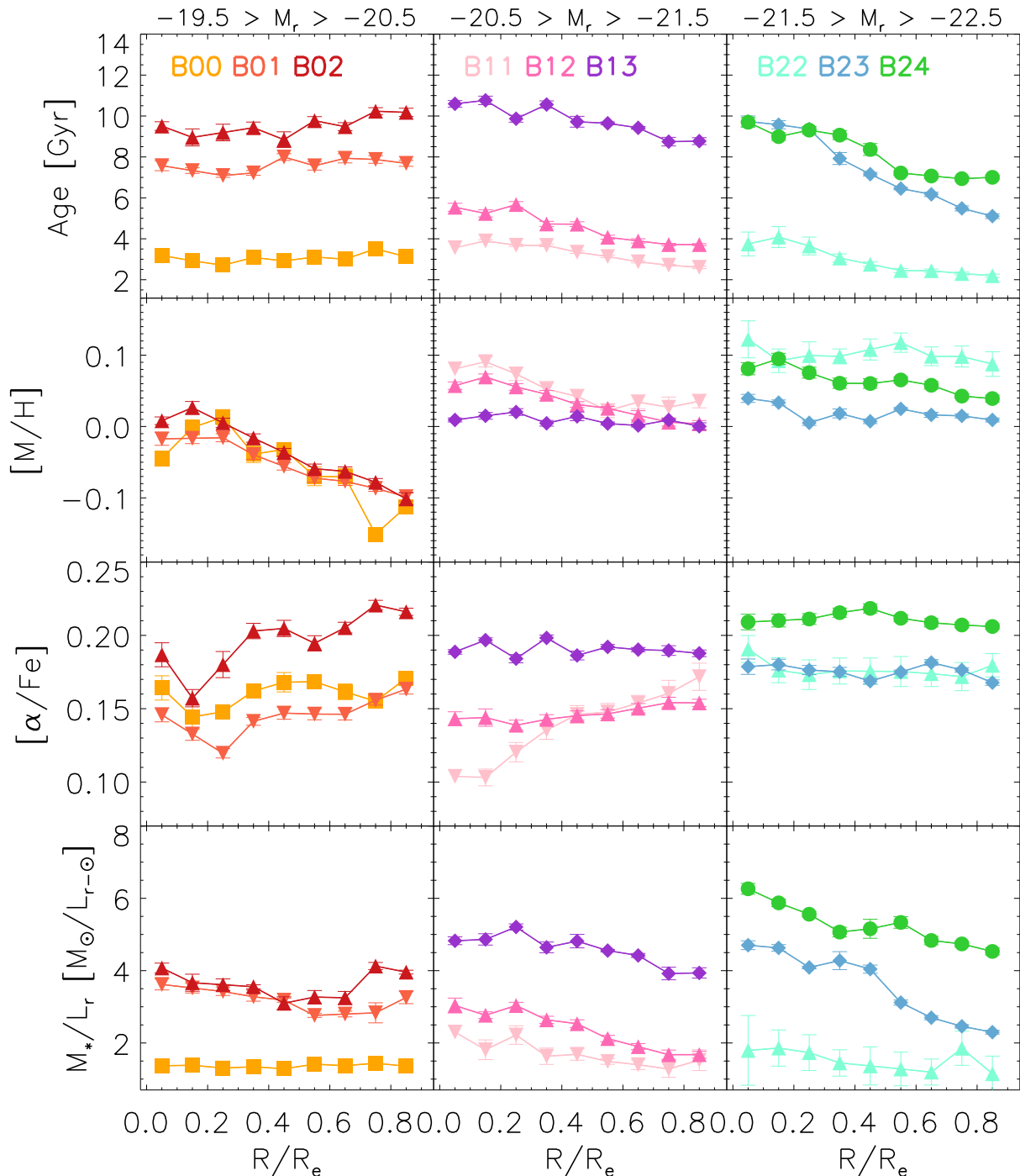


Figure 10. Age, metallicity, α -enhancement and M_*/L versus R/R_e , when the IMF is allowed to vary. Each column shows bins in the same luminosity range. Colors and symbols as in Figure 9.

bins (e.g., B01, B02, B12) and almost negligible for others (e.g., B00, B22).

Figure 9 compares the best-fitting SP parameters as a function of velocity dispersion when the IMF is allowed to vary and when it is fixed (to Kroupa). The IMF variations have an important effect in the inferred M_*/L_r values, which affect both stellar mass estimates – M_{dyn} and M_* – as we stressed in Papers I and II. However, the effect of the IMF on the other SP parameters is much weaker, and the overall shape and relative values between bins remain almost

unchanged. This figure highlights the relation between the velocity dispersion gradient and those in age and metallicity: the low luminosity bins (red, orange and yellow) show relatively flat velocity and age profiles, while in the other bins the velocity and age gradients are stronger. The metallicity gradients are strongest for the lowest luminosity bins, weaker for intermediate luminosities, and almost flat for the most luminous ones. We discuss these trends in Section 6.

Figure 10 shows how the SP estimates shown in the left hand panels of Figure 9 (i.e. when allowing for IMF varia-

tions) change with galactocentric distance (rather than σ). Except for M_*/L_r , fixing the IMF to Kroupa makes little difference.) To simplify the comparison, bins of different luminosities are plotted separately in each column. It is evident that, at fixed M_r , age increases with σ_0 while metallicity decreases (except at $M_r > -20.5$, where the values are very similar). Stated differently, at fixed σ_0 , more luminous galaxies are younger and more metal rich (compare upright triangles in the three top panels, or the upside-down triangles in the left and middle panels). Evidently, the usual statement that ‘massive galaxies are older’ (c.f. Introduction) is not true if σ_0 is held fixed.

Regarding the α -enhancement, at fixed luminosity, $[\alpha/\text{Fe}]$ decreases with σ_0 (compare purple and light pink tracks), but become very similar for the lowest σ_0 bins at each M_r (e.g., compare cyan and blue). The α -enhancement profiles are almost flat for all the bins, except for bins B02 (red) and B11 (light pink), which show positive gradients. Finally, the bottom panels show that, at fixed L , M_*/L increases with σ_0 but gradients are stronger for the more luminous S0s.

In Figures 9 and 10 the error bars show the 1σ variation in the best-fitting parameters after bootstrapping one galaxy at a time when constructing the stacked spectra. These uncertainties are significantly smaller than any systematics due to the use of different SSP models, IMF parametrizations, or IMF indicators. They are even smaller than the differences due to normalising the stacks in different spectral regions. Therefore, while we are very confident of our stacking procedure, we warn the reader about the other assumptions which can affect the results presented here.

4 ARE FAST ROTATOR ELLIPTICALS JUST FACE-ON S0 GALAXIES?

So far we have concentrated on the properties of S0s. As we noted in the Introduction, whether or not S0s, which are almost exclusively fast rotators, are fundamentally different from fast rotating Es is an open question. Recent work asserts that E-FRs are just S0s viewed face-on (e.g. Cappellari 2016; Graham et al. 2019). In this section we compare kinematic profiles and SPs of S0s and E-FRs of the same luminosity and velocity dispersion. Comparison of the left and right hand panels of Figure 2 shows the region in the M_r - σ_0 plane where there is sufficient overlap to perform this comparison. This is only possible for bins B12, B13, B23 and B24.

Whereas the reason for comparing the SPs is self-evident, our motivation for comparing kinematics deserves further comment. Traditionally, S0s are thought to differ from Es because they have obvious inner dispersion supported bulge and outer rotation supported disc components. In IFU datasets, this means that rotation should be obvious in the outer regions of S0s, provided they are not viewed face-on. If face-on, then this rotation should be less obvious. Moreover, the velocity dispersion in the outer parts, where the disc dominates, should be small, because we expect discs to be somewhat ‘cold’. In contrast, morphologically, E-FRs do not have an obvious disc component. Therefore, there is no particular reason to expect the velocity dispersion profiles of E-FRs to differ from those of E-SRs. Therefore, compar-

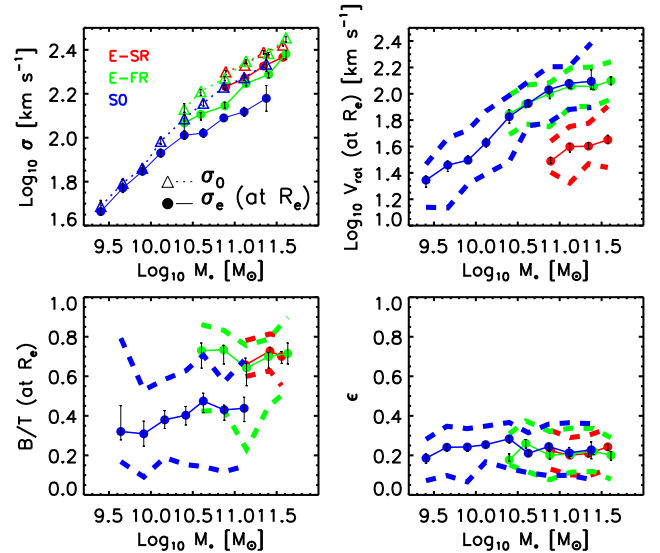


Figure 11. Velocity dispersion (central and at R_e), rotation speed, B/T and ϵ shown as median and quartiles as a function of stellar mass for E-SRs (red), E-FRs (green) and S0s with $\epsilon < 0.4$ (blue).

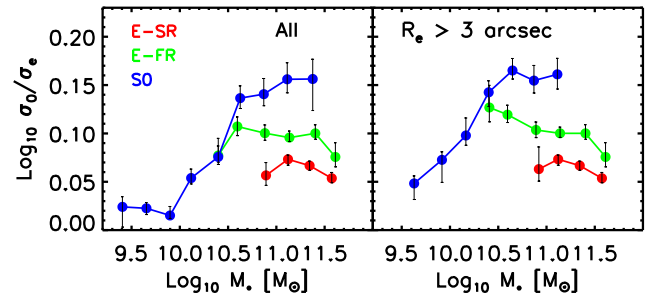


Figure 12. Ratio of central σ_0 to σ_e (the values shown in the top left panel of the previous Figure) for S0s (blue) E-FRs (green) and E-SRs (red) as a function of stellar mass, for the full sample (left) and when restricted to objects with $R_e > 3$ arcsec (right).

ing the rotation and velocity dispersion profiles of E-FRs and face-on S0s of similar L and σ_0 may be useful.

4.1 Velocity dispersion profiles

To explore this, we first select from our E and S0 samples only those objects which have $\epsilon < 0.4$ (so face-on objects are a greater fraction). Figure 11 shows how some kinematic (top panels) and photometric (bottom) properties of the objects which satisfy this cut vary with stellar mass. The solid curves in the bottom right panel show that the median ϵ is similar for all three morphological types. The associated dashed curves show that the quartiles around the median are also similar. The bottom left panel shows that the E-SR and E-FR samples have similar median B/T values of about 0.7, whereas the S0s have a smaller median B/T, with a small but statistically significant step at $3 \times 10^{10} M_\odot$. S0s with B/T values above their median overlap with E-FRs that lie below their median. The top right panel shows that E-FRs and S0s

have very similar rotation speeds which are, of course, much larger than for E-SRs. Finally, the top left panel shows that E-FRs have central velocity dispersion σ_0 similar to E-SRs and slightly larger than S0s of the same M_* . The difference between S0s and the Es is slightly larger for σ_e (at, not within, R_e), in qualitative agreement with the discussion in the previous paragraph. (Rotation does not contribute to either of the estimated σ s.)

As we noted above, we are particularly interested in the slope of the velocity dispersion profile. Figure 12 shows a crude measure of this slope – the ratio σ_0/σ_e – for the three morphological types, as a function of M_* . At high masses, where a comparison is possible, this ratio is largest for S0s and smallest for E-SRs. Evidently, the velocity dispersion drops more steeply for (face-on) S0s than it does for Es.

To check if the fiber size (radius ~ 1 arcsec) is compromising our results, the right-hand panel shows the result of restricting the analysis to objects having $R_e > 3$ arcsecs, for which the aperture of the fiber should matter less. Comparison of the two panels shows that, while there are some differences at smaller masses, over the range where all the morphological types can be compared, the differences are robust. (Restricting to $R_e > 4$ arcsecs reduces the sample size considerably but does not change our conclusions.) The steeper σ profiles for S0s, despite similar rotation speeds (see top right panel of Figure 11), indicate that S0s tend to be more rotationally supported than are E-FRs.

It is worth noting that, for S0s, both B/T and the σ_0/σ_e ratio change dramatically around $3 \times 10^{10} M_\odot$, the same mass scale where their stellar population gradients change. Some of the drop and leveling-off in σ_0/σ_e at low M_* may be artificial, because both values are close to the instrumental resolution of the spectrograph (~ 60 km/s, see top left panel of Figure 11). While this resolution has been accounted-for in our measurements, the σ estimates become increasingly uncertain below this value. Of course, this does not affect our conclusions about the differences between S0s and E-FRs at higher masses.

Before moving on to consider the stellar populations, it is natural to ask if the difference in velocity dispersion profiles is simply due to differences in B/T ratio. The bottom left panel of Figure 11 shows that, at fixed M_* , S0s have smaller B/T than E-FRs, so one would expect S0s to have steeper velocity dispersion profiles. However, the Figures show that at fixed morphology, the B/T– M_* and σ_0/σ_e – M_* correlations are both flat (above $3 \times 10^{10} M_\odot$). As a result, it is not obvious that B/T drives the differences we see in Figure 12. Indeed, if we only select objects with $0.45 < \text{B/T} < 0.6$ and $10.5 < \log_{10}(M_*/M_\odot) < 11$ then S0s and E-FRs have $\log_{10}(\sigma_0/\sigma_e) \approx 0.1$ and 0.15 , just as in Figure 12. Unfortunately, there are so few objects in this bin that it is hard to make a more statistically significant statement.

4.2 Stellar population gradients

We now consider the stellar populations. We estimate SP parameters of the Es exactly as we did for S0s in Section 3 and note that although our results allow IMF variations, fixing the IMF to Kroupa results in small quantitative changes, but does not change any of the qualitative trends or conclusions.

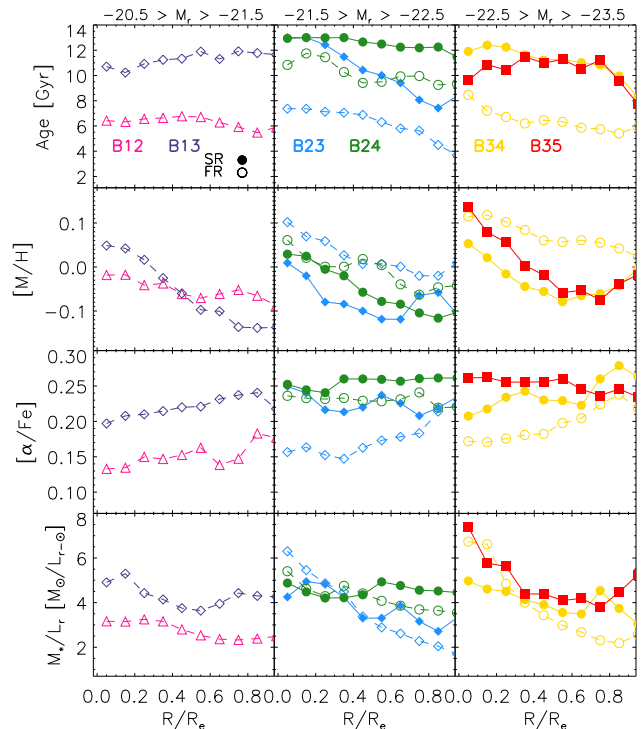


Figure 13. Age, metallicity, α -enhancement and M_*/L_* versus R/R_e for the E-SRs and E-FRs (filled and open symbols) when allowing for IMF variations. Colors represent the different bins as stated in the legend, and symbol shape represents σ_0 .

Figure 13 shows the results: E-SRs (filled symbols) tend to be older, more metal poor (less metal rich) and more α -enhanced than E-FRs (open symbols) of the same M_r and σ_0 . In addition, the left and middle panels show that at fixed M_r , E-FRs with large σ_0 are older, more metal rich (at least in the central regions) and more α -enhanced. Stated differently, at fixed σ_0 , the fainter E-FRs are older, less metal rich and more α -enhanced. These trends are not so obvious, or simply absent for E-SRs. However, these SP trends for E-FRs are rather similar to those of S0s.

Figure 14 presents a direct comparison of the S0s and E-FRs (symbols connected by solid and dashed lines respectively) in bins B12, B13, B23 and B24. In all but one bin (B23), the S0s tend to be younger and more metal rich. They also tend to be slightly less α -enhanced. These differences, which are also present if we fix the IMF to Kroupa, are noteworthy, given that they played no role in the morphological classifications.

Figure 15 shows these SP differences in a slightly different format. The four sets of curves show the joint distribution of age and metallicity from the center (symbols) outwards (tails) for S0s (solid) and E-FRs (dotted) in bins B12, B13, B23 and B24. This shows that S0s tend to have larger age gradients than their corresponding E-FRs; in contrast, the E-FRs tend to have larger metallicity gradients. In Paper II we showed that E-SRs tend to have constant ages (of about 10 Gyrs) with some metallicity gradients, so old E-FRs (bins B13 and B24) are more similar to E-SRs than are S0s. These systematic SP differences, along with the differences shown in Figure 12, suggest that, contrary

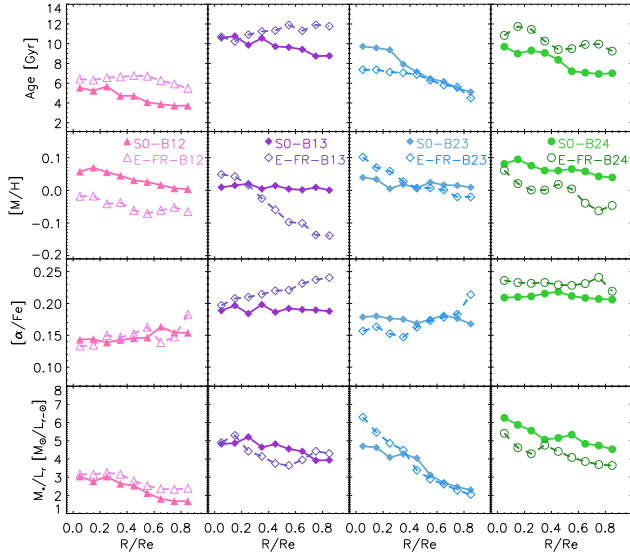


Figure 14. Comparison of the stellar populations of S0s (filled symbols and solid lines) and E-FRs (open symbols and dashed lines) of the same M_r and σ_0 , for a range of values of M_r and σ_0 . The two panels on the left are fainter than the two on the right, and σ_0 increases from left to right, except that σ_0 is the same for the two middle panels.

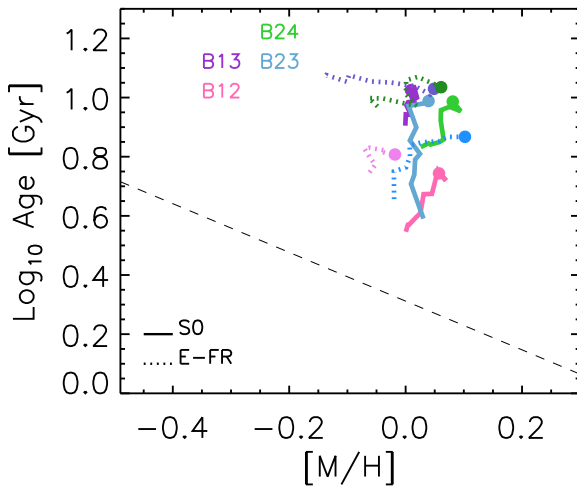


Figure 15. Joint age-metallicity gradients of S0s (solid) and E-FRs (dotted) for the four bins where there is sufficient overlap between the populations (ages and metallicities are same as Figure 14). These S0s tend to have stronger age gradients, whereas the corresponding E-FRs tend to have stronger metallicity gradients.

to recent claims (e.g. Cappellari 2016; Graham et al. 2019), E-FRs are not just S0s viewed face-on.

If inclination does not drive the differences between them, then what does? If bulges are dispersion supported and older than disks (which are supported by rotation), then we would expect differences in B/T ratio to be reflected in the kinematic and stellar population gradients. While E-FRs do have larger B/T (Figure 11), our sample is too small to allow us to test if B/T alone drives the kinematic and SP trends we see.

5 COMPARISON WITH PREVIOUS WORK

Previous work, based on the joint distribution of color, luminosity and velocity dispersion has argued that residuals from the $\sigma_0 - L$ relation must be age indicators (Bernardi et al. 2005). The sense of the age correlation is that at fixed luminosity, older galaxies have larger σ_0 ; at fixed σ_0 , older galaxies are fainter (also see Figure 1 of Shankar & Bernardi 2009). Our Figures 5 and 10 show that this is abundantly true for S0s. Paper II did not explore a large enough range of L_r to test if this is also true for Es. Figure 13 shows that it is, at least for Es that are fast rotators.

The properties of 279 MaNGA S0 galaxies have previously been studied by FM2018. They estimate stellar ages and metallicities in bulge and disk regions of individual galaxies, and report a bimodality which strongly correlates with stellar mass: high-mass ($M_* > 10^{10} M_\odot$) S0s are old and metal-rich, with older bulge components; low-mass lenticulars are young and metal-poor without significant differences in the properties of their disk and bulge components.

As we now discuss, our results are in general agreement with theirs, despite significant differences in how we estimate SP parameters. However, there are a few subtle but important differences which we highlight below.

The first potentially important difference is in the morphological classification. FM2018 selected S0 galaxies according to two conditions: galaxies with Galaxy Zoo2 (Willett et al. 2013; Hart et al. 2016) weighted ‘smooth’ fraction > 0.7 and fast rotating, without any further restriction in luminosity. However, the MDLM-VAC we use here classifies only 45% of their sample as S0; it classifies 30% of their sample as Es and 25% as Spirals (see top panel of Figure 24 in Fischer et al. 2019, which shows that Galaxy Zoo2 smooth fraction is not good at discriminating between S0 and other morphologies). Figure 25 of Fischer et al. (2019) shows that many of the objects with smooth fraction > 0.7 have Sersic index and bulge fraction values that are consistent with being Spirals, and these are indeed classified as Spirals by the MDLM-VAC. Figure A4 shows a selection of these objects.

To see how this affects the conclusions of FM2018, Figure 16 shows how the Spirals, S0s and E-FRs (as classified by the MDLM-VAC) in their sample populate the age-metallicity plane, in the format of their Figure 10, for a number of bins in luminosity. Magenta lines connect bulges to their disks if the bulge is more than 0.1 dex older, otherwise the line is black. Comparison of the panels shows that the vast majority of the fainter, younger, metal-poor objects which make up FM2018’s ‘second’ population are objects classified as Spirals in the MDLM-VAC. While some of the fainter S0s ($M_r < -20.5$) lie below the dashed line, they are a small fraction of the faint S0s, and so an even smaller fraction of all S0s. Essentially none of the E-FRs lie below the dashed line. Evidently, the bimodality reported by FM2018 is primarily due to morphology, rather than luminosity.

Although it is clearly evident in their Figure 10 (and hence in our Figure 16), FM2018 do not comment on a different sort of bimodality: Whereas the disks and bulges of massive S0s have essentially the same metallicities (but different ages), the metallicities of disks and bulges can be quite different at lower masses. We expect this difference to be quite dramatic in our sample, because Figures 9 and 10 show that the SP gradients of faint and luminous S0s are

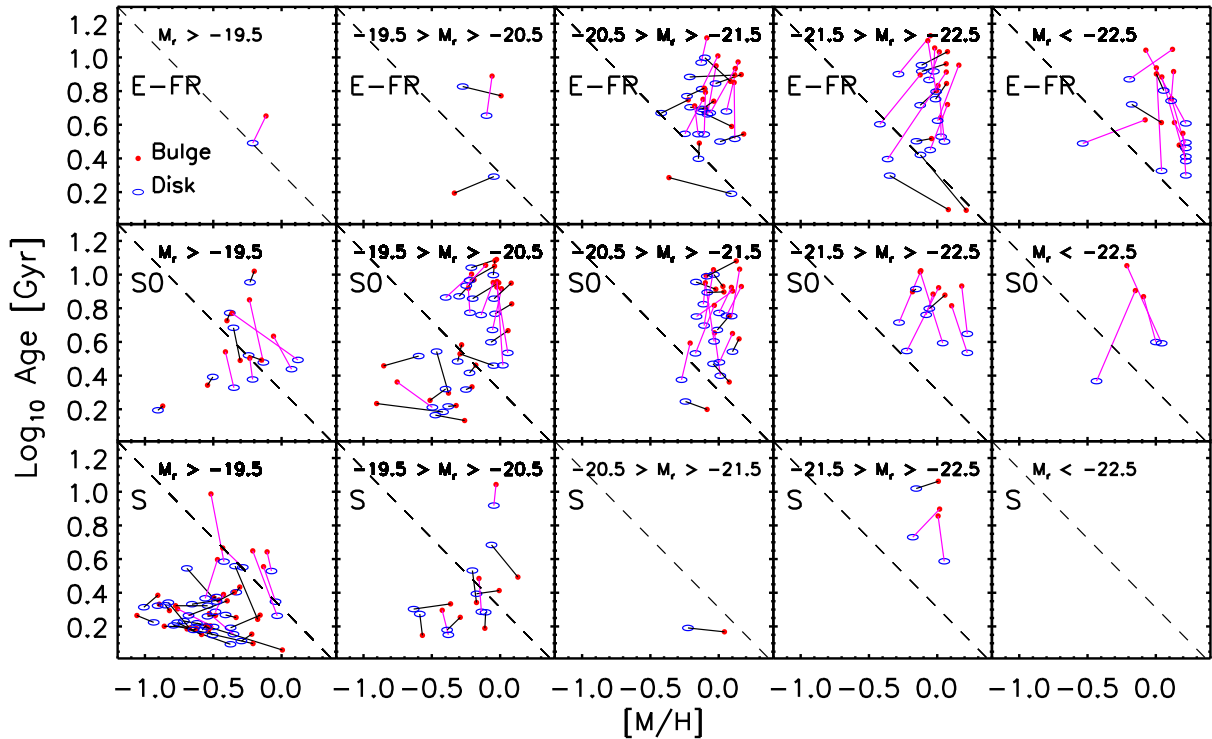


Figure 16. Ages and metallicities for the bulge and disk components of the objects in the sample studied by FM2018, separated according to MDLM-VAC morphology and luminosity: Bottom to top shows Spirals, S0s and E-FRs, and luminosity increases from left to right. The three middle luminosity bins are the same as those we focus on in this paper. Magenta lines connect bulges to their disks if the bulge is more than 0.1 dex older, otherwise the line is black. Dashed line, same in all panels, approximately separates the two populations found by FM2018.

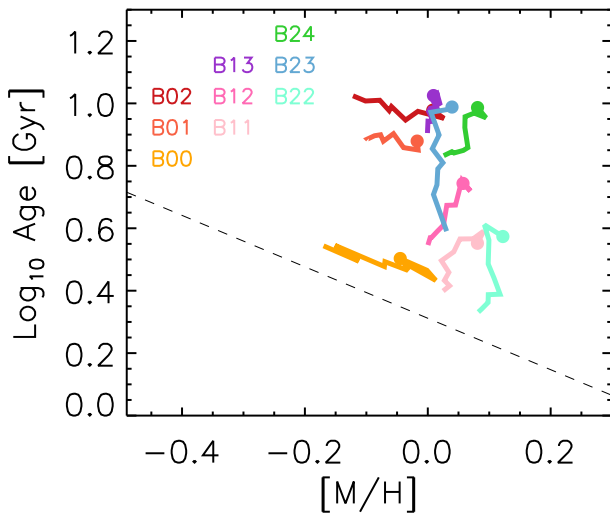


Figure 17. Comparison of age-metallicity gradients of S0s in the nine bins defined in Table 3, color coded as in the previous figures. Filled circles indicate the central region. Fainter objects tend to have large metallicity gradients but weak age gradients; luminous objects tend to have large age gradients but weak metallicity gradients.

very different. To illustrate, Figure 17 shows how the SP gradients we measure in our nine bins populate the age-metallicity plane. Notice the nearly horizontal stripes in the low L bins (centers are less metal poor and very slightly younger – similar to most faint Spirals in Figure 16), but

vertical stripes at high luminosities (centers are substantially older and only slightly more metal rich, similar to the E-FRs in Figure 16). This clear bimodality in S0 properties is obvious even though we are restricting our analysis to the upper end of the mass range covered by FM2018. (Their bimodality, which Figure 16 suggests is driven by morphology, only really manifests at $M_r > -20$ or fainter.)

6 DISCUSSION AND CONCLUSIONS

We used stacked spectra to study how the kinematics of and chemical abundances in S0 galaxies vary with velocity dispersion and luminosity (Figure 2). We interpreted the chemical abundances using (MILES bimodal) single stellar population models.

- Our analysis has uncovered a bimodality in the S0 population. The correlations between size or velocity dispersion and stellar mass change slope at around $3 \times 10^{10} M_{\odot}$ (left hand panel of Figure 1). This coincides with the mass scale at which gradients in kinematics and stellar population change dramatically. In particular, there are obvious gradients in line-index strength (Figures 5–7) which also change at this mass scale. When fit to our measurements, single stellar population models indicate that the more massive S0s show strong age gradients but little or no metallicity gradient, while the less massive ones present relatively flat age and velocity dispersion profiles, but a significant metallicity gradient (Figure 17).

- S0s with the smallest σ_0 in each luminosity bin – i.e.,

the youngest S0s for their L_r – have IMFs that are closest to Kroupa (Figure 8) – but IMFs are otherwise a little more bottom heavy. (We accounted self-consistently for IMF differences when estimating other SP parameters, which are all light- not mass-weighted.)

- While at fixed L_r , age increases with σ_0 and metallicity decreases as expected, we find that, at fixed σ_0 , more luminous S0s are younger, more metal rich and less α -enhanced (compare same symbols in the different panels of Figure 10). Evidently, the usual statement that ‘massive galaxies are older’ is not true if σ_0 is held fixed.

- We also found differences between the kinematic profiles and stellar populations of the S0 and E-FR populations. The velocity dispersion profiles of (face-on) S0s are steeper than those of E-FRs (Figure 12), despite the fact that both populations have similar rotation (top right panel of Figure 11). This indicates that S0s tend to be less supported by dispersion than are E-FRs. Like S0s – but in contrast to E-SRs – at fixed σ_0 , more luminous E-FRs are younger and more metal rich (Figure 13). However, their gradients differ: S0s tend to have larger age gradients and smaller metallicity gradients than E-FRs of the same L and σ_0 (Figure 15). The age-metallicity gradients of E-FRs are more similar to those of E-SRs. Together, these SP and kinematic differences suggest that distinguishing between E-FRs and S0s is meaningful: E-FRs are not just S0s viewed face-on. While E-FRs tend to have larger B/T ratios (bottom left panel of Figure 11), our sample is not large enough to determine if the differences between E-FRs and S0s are entirely driven by B/T.

Gradient strength is thought to be an indicator of the interplay between star formation and stellar mass assembly. The qualitative change in gradients that we see in the S0 population, coupled with the change in global scaling relations at $M_* \sim 3 \times 10^{10} M_\odot$, suggest that this is a special scale for S0s. It is tempting to assert that, below this mass scale, S0s are closer to Spirals – mergers are less important than in situ star formation and perhaps, some gentle gas stripping. These galaxies have metallicity gradients but little age gradient. They also have similar metallicities but with the larger σ S0s being older and more α -enhanced. However, the transition from metallicity to age gradients just above this mass scale suggests gas rich mergers are beginning to matter, as these would result in more recent star formation from enriched gas, and hence younger light-weighted ages with higher metallicity and smaller α -enhancement – this would explain why at fixed σ_0 , more luminous S0s and E-FRs are younger, more metal rich and less α -enhanced (compare same symbols in the different panels of Figure 10). In addition, if the merger remnant is able to grow a disc, it will have higher metallicity, younger age and lower $[\alpha/\text{Fe}]$ in its outer regions compared to its progenitors, thus explaining the change in S0 gradients we see as we cross $M_* \sim 3 \times 10^{10} M_\odot$ (Figure 17).

Mergers increase the stellar mass, but the abundance of S0s drops sharply above $2 \times 10^{11} M_\odot$ (Figure 1); this mass scale was first identified as being important by Bernardi et al. (2011). More recent work (Cappellari et al. 2013, and our Papers I and II) has confirmed its significance. At these higher masses there is a mix of E-FRs and E-SRs. E-FRs may result from mergers which do not produce discs, or for which a disc would have been unstable. Younger E-FRs (pink

and blue dotted lines in Figure 15) have age-metallicity gradients which are intermediate between those of S0s and older Es (Figure 13). Older E-FRs (purple and green dotted lines in Figure 15) have metallicity decreasing outwards from the center, but little if any age gradient within R_e . This is similar to E-SRs – which are uniformly old, have metallicity gradients and are thought to be dominated by dry merger assembly histories. However, these E-FRs tend to be younger, more metal rich and less α -enhanced than E-SRs of the same L and σ_0 (Figure 13 and Paper II), consistent with E-FRs having had more extended star formation histories.

ACKNOWLEDGEMENTS

We are grateful to the referee for a helpful report, and to A. Fraser McKelvie for sharing the data used in FM2018. This work was supported in part by NSF grant AST-1816330. HDS acknowledges support from Centro Superior de Investigaciones Científicas PIE2018-50E099. FN acknowledges support from the National Science Foundation Graduate Research Fellowship (NSF GRFP) under Grant No. DGE-1845298.

Funding for the Sloan Digital Sky Survey IV has been provided by the Alfred P. Sloan Foundation, the U.S. Department of Energy Office of Science, and the Participating Institutions. SDSS acknowledges support and resources from the Center for High-Performance Computing at the University of Utah. The SDSS web site is www.sdss.org.

SDSS is managed by the Astrophysical Research Consortium for the Participating Institutions of the SDSS Collaboration including the Brazilian Participation Group, the Carnegie Institution for Science, Carnegie Mellon University, the Chilean Participation Group, the French Participation Group, Harvard-Smithsonian Center for Astrophysics, Instituto de Astrofísica de Canarias, The Johns Hopkins University, Kavli Institute for the Physics and Mathematics of the Universe (IPMU) / University of Tokyo, Lawrence Berkeley National Laboratory, Leibniz Institut für Astrophysik Potsdam (AIP), Max-Planck-Institut für Astronomie (MPIA Heidelberg), Max-Planck-Institut für Astrophysik (MPA Garching), Max-Planck-Institut für Extraterrestrische Physik (MPE), National Astronomical Observatories of China, New Mexico State University, New York University, University of Notre Dame, Observatorio Nacional / MCTI, The Ohio State University, Pennsylvania State University, Shanghai Astronomical Observatory, United Kingdom Participation Group, Universidad Nacional Autónoma de México, University of Arizona, University of Colorado Boulder, University of Oxford, University of Portsmouth, University of Utah, University of Virginia, University of Washington, University of Wisconsin, Vanderbilt University, and Yale University.

REFERENCES

- Aguado D. S., et al., 2019, *ApJS*, **240**, 23
 Barway S., Kembhavi A., Wadadekar Y., Ravikumar C. D., Mayya Y. D., 2007, *ApJ*, **661**, L37
 Barway S., Wadadekar Y., Kembhavi A. K., Mayya Y. D., 2009, *MNRAS*, **394**, 1991

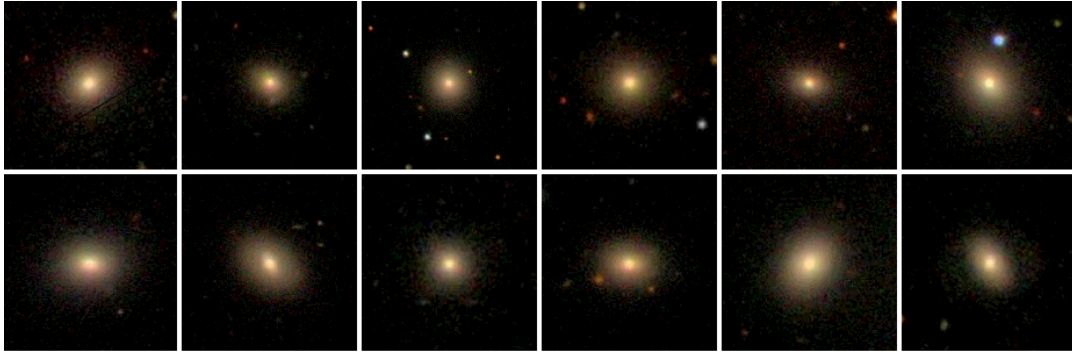


Figure A1. Random selection of objects which we classify as E-SRs in the two luminosity bins in common with the S0 sample: $-20.5 > M_r > -21.5$ (top) and $-19.5 > M_r > -20.5$ (bottom).

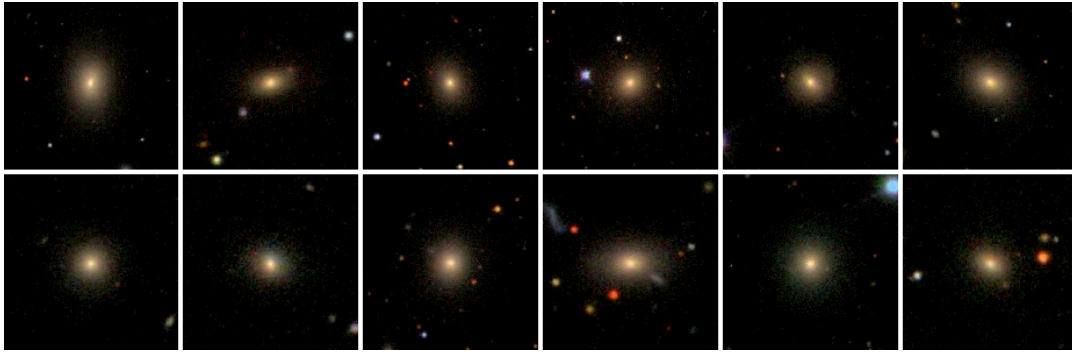


Figure A2. Same as previous figure, but for E-FRs.



Figure A3. Random selection of objects which we classify as S0s in the three luminosity bins used for our analysis: $-20.5 > M_r > -21.5$ (top) and $-19.5 > M_r > -20.5$ (middle) and $-19.5 > M_r > -20.5$ (bottom).

Bernardi M., Sheth R. K., Nichol R. C., Schneider D. P., Brinkmann J., 2005, *AJ*, **129**, 61
 Bernardi M., Nichol R. C., Sheth R. K., Miller C. J., Brinkmann J., 2006, *AJ*, **131**, 1288
 Bernardi M., Roche N., Shankar F., Sheth R. K., 2011, *MNRAS*, **412**, L6
 Bernardi M., Domínguez Sánchez H., Brownstein J. R., Drory N., Sheth R. K., 2019, *MNRAS*, **489**, 5633
 Blanton M. R., et al., 2017, *AJ*, **154**, 28
 Bundy K., et al., 2015, *ApJ*, **798**, 7
 Cappellari M., 2016, *ARA&A*, **54**, 597

Cappellari M., et al., 2013, *MNRAS*, **432**, 1862
 Conroy C., Villaume A., van Dokkum P. G., Lind K., 2018, *ApJ*, **854**, 139
 Domínguez Sánchez H., Huertas-Company M., Bernardi M., Tuccillo D., Fischer J. L., 2018, *MNRAS*, **476**, 3661
 Domínguez Sánchez H., Bernardi M., Brownstein J. R., Drory N., Sheth R. K., 2019, *MNRAS*, **489**, 5612
 Drory N., et al., 2015, *AJ*, **149**, 77
 Emsellem E., et al., 2007, *MNRAS*, **379**, 401
 Ferreras I., et al., 2019, *MNRAS*, **489**, 608
 Fischer J.-L., Domínguez Sánchez H., Bernardi M., 2019, *MN-*

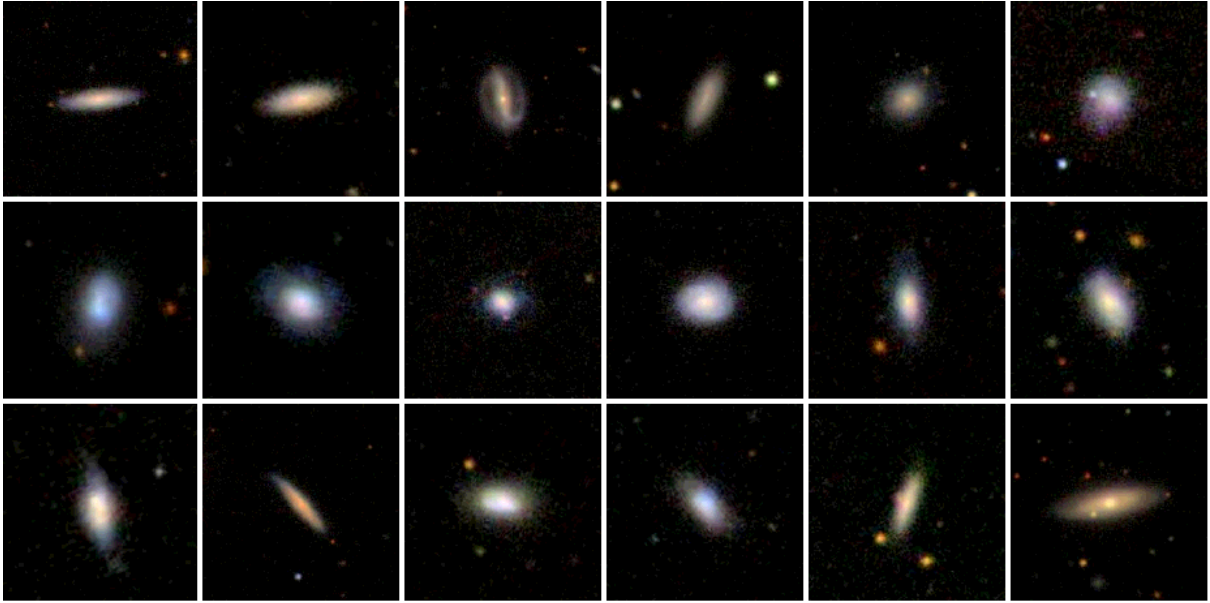


Figure A4. Random selection of objects which FM2018 classify as S0s but we classify as Spirals. A considerable fraction of these objects are indeed Spirals.

[RAS](#), [483](#), [2057](#)

Fraser-McKelvie A., Aragón-Salamanca A., Merrifield M., Tabor M., Bernardi M., Drory N., Parikh T., Argudo-Fernández M., 2018, [MNRAS](#), [481](#), [5580](#)

Graham M. T., et al., 2018, [MNRAS](#), [477](#), [4711](#)

Graham M. T., Cappellari M., Bershady M. A., Drory N., 2019, arXiv e-prints, p. [arXiv:1910.05136](#)

Gunn J. E., et al., 2006, [AJ](#), [131](#), [2332](#)

Hart R. E., et al., 2016, [MNRAS](#), [461](#), [3663](#)

Kauffmann G., et al., 2003, [MNRAS](#), [341](#), [33](#)

Kroupa P., 2001, [MNRAS](#), [322](#), [231](#)

La Barbera F., Ferreras I., Vazdekis A., de la Rosa I. G., de Carvalho R. R., Trevisan M., Falcón-Barroso J., Ricciardelli E., 2013, [MNRAS](#), [433](#), [3017](#)

Lacerna I., Ibarra-Medel H., Avila-Reese V., Hernández-Toledo H. M., Vázquez-Mata J. A., Sánchez S. F., 2020, arXiv e-prints, p. [arXiv:2001.05506](#)

Law D. R., et al., 2015, [AJ](#), [150](#), [19](#)

Law D. R., et al., 2016, [AJ](#), [152](#), [83](#)

Mendel J. T., Simard L., Palmer M., Ellison S. L., Patton D. R., 2014, [ApJS](#), [210](#), [3](#)

Panther B., Jimenez R., Heavens A. F., Charlot S., 2007, [MNRAS](#), [378](#), [1550](#)

Parikh T., et al., 2019, [MNRAS](#), [483](#), [3420](#)

Shankar F., Bernardi M., 2009, [MNRAS](#), [396](#), [L76](#)

Smee S. A., et al., 2013, [AJ](#), [146](#), [32](#)

Tang B., Worthey G., 2017, [MNRAS](#), [467](#), [674](#)

Thomas D., Maraston C., Bender R., Mendes de Oliveira C., 2005, [ApJ](#), [621](#), [673](#)

Thomas D., Maraston C., Johansson J., 2011, [MNRAS](#), [412](#), [2183](#)

Trager S. C., Worthey G., Faber S. M., Burstein D., González J. J., 1998, [ApJS](#), [116](#), [1](#)

Vazdekis A., Sánchez-Blázquez P., Falcón-Barroso J., Cenarro A. J., Beasley M. A., Cardiel N., Gorgas J., Peletier R. F., 2010, [MNRAS](#), [404](#), [1639](#)

Vazdekis A., et al., 2015, [MNRAS](#), [449](#), [1177](#)

Wake D. A., et al., 2017, [AJ](#), [154](#), [86](#)

Westfall K. B., et al., 2019, arXiv e-prints,

Willett K. W., et al., 2013, [MNRAS](#), [435](#), [2835](#)

Worthey G., 1994, [ApJS](#), [95](#), [107](#)

Yan R., et al., 2016a, [AJ](#), [151](#), [8](#)

Yan R., et al., 2016b, [AJ](#), [152](#), [197](#)

APPENDIX A: IMAGES

Morphology plays an important role in our sample selection. This Appendix shows a random selection of objects to illustrate that our morphological classifications are reasonable. Comparison of Figures [A1](#) and [A2](#) shows that E-SRs and E-FRs are very similar morphologically, whereas comparison of Figures [A2](#) and [A3](#) shows that S0s tend to have more obvious disks.

Finally, Figure [A4](#) shows a random selection of objects which FM2018 classify as S0s but we classify as Spirals. A considerable fraction of these objects are indeed Spirals, suggesting that the FM2018 S0 sample is rather impure. As not all of these objects are obviously Spirals, our S0 sample may be slightly incomplete. However, we believe it is much more pure.

This paper has been typeset from a $\text{\TeX}/\text{\LaTeX}$ file prepared by the author.